APL Materials

Pulsed-laser epitaxy of metallic delafossite $PdCrO_2$ films

Cite as: APL Mater. **8**, 051104 (2020); https://doi.org/10.1063/1.5144743
Submitted: 10 January 2020 . Accepted: 08 April 2020 . Published Online: 04 May 2020

Jong Mok Ok, Matthew Brahlek, Woo Seok Choi, Kevin M. Roccapriore, Matthew F. Chisholm, Soyeun Kim, Changhee Sohn, Elizabeth Skoropata, Sangmoon Yoon, Jun Sung Kim, and Ho Nyung Lee

Pulsed-laser epitaxy of metallic delafossite $PdCrO_2$ films

Cite as: APL Mater. 8, 051104 (2020); doi: 10.1063/1.5144743
Submitted: 10 January 2020 • Accepted: 8 April 2020 •
Published Online: 4 May 2020

Jong Mok Ok,[1] Matthew Brahlek,[1] Woo Seok Choi,[2] Kevin M. Roccapriore,[3] Matthew F. Chisholm,[3] Soyeun Kim,[4] Changhee Sohn,[1,4] Elizabeth Skoropata,[1] Sangmoon Yoon,[1] Jun Sung Kim,[5,6] and Ho Nyung Lee[1,a)]

AFFILIATIONS

[1]Materials Science and Technology Division, Oak Ridge National Laboratory, Oak Ridge, Tennessee 37831, USA
[2]Department of Physics, Sungkyunkwan University, Suwon 16419, South Korea
[3]Center for Nanophase Materials Sciences, Oak Ridge National Laboratory, Oak Ridge, Tennessee 37831, USA
[4]Department of Physics, Ulsan National Institute of Science and Technology, Ulsan 44919, South Korea
[5]Department of Physics, Pohang University of Science and Technology, Pohang, South Korea
[6]Center for Artificial Low Dimensional Electronic Systems, Institute for Basic Science (IBS), Pohang, South Korea

[a)]**Author to whom correspondence should be addressed:** hnlee@ornl.gov

ABSTRACT

Alternate stacking of a highly conducting metallic layer with a magnetic triangular layer found in delafossite $PdCrO_2$ provides an excellent platform for discovering intriguing correlated quantum phenomena. Thin film growth of delafossites may enable not only the tuning of the basic physical properties beyond what bulk materials can exhibit, but also the development of novel hybrid materials by interfacing with dissimilar materials, yet this has proven to be extremely challenging. Here, we report the epitaxial growth of metallic delafossite $PdCrO_2$ films by pulsed laser epitaxy (PLE). The fundamental role of the PLE growth conditions, epitaxial strain, and chemical and structural characteristics of the substrate is investigated by growing under various growth conditions and on various types of substrates. While strain plays a large role in improving the crystallinity, the direct growth of epitaxial $PdCrO_2$ films without impurity phases was not successful. We attribute this difficulty to both the chemical and structural dissimilarities with the substrate and volatile nature of the PdO sublayer, which make nucleation of the right phase difficult. This difficulty was overcome by growing $CuCrO_2$ buffer layers before $PdCrO_2$ films were grown. Unlike $PdCrO_2$, $CuCrO_2$ films were readily grown with a relatively wide growth window. Only a monolayer thick buffer layer was sufficient to grow the correct $PdCrO_2$ phase. This result indicates that the epitaxy of Pd-based delafossites is extremely sensitive to the chemistry and structure of the interface, necessitating near perfect substrate materials. The resulting films are commensurately strained and show an antiferromagnetic transition at 40 K that persists down to as thin as 3.6 nm in thickness. This work provides key insights into advancing the epitaxial growth of the broader class of metallic delafossites for both studying the basic physical properties and developing new spintronic and computing devices.

ABO_2 delafossites are a class of materials offering a wide range of fascinating physical properties due to the inherent combination of electronic conduction and magnetism.[1,2] Unique to this class of materials is the layered structure consisting of alternating A and BO_2 layers as shown in Fig. 1(a). The natural heterostructuring of the A and BO_2 layers makes delafossites highly attractive to study the itinerate behaviors of electrons combined with localized non-collinear magnetism. In addition, the intrinsically long mean free path leading to an extremely high conductivity as well as the two-dimensional (2D) nature of the transport merit this material system for transformative applications.[3,4] The A layer is composed of closed-packed cations with A = Cu, Pd, Ag, or Pt, whereas the BO_2 layer is composed of slightly distorted edge-sharing BO_6 octahedra with B = Al, Cr, Fe, Co, or Rh.[1,2,5] The delafossites with

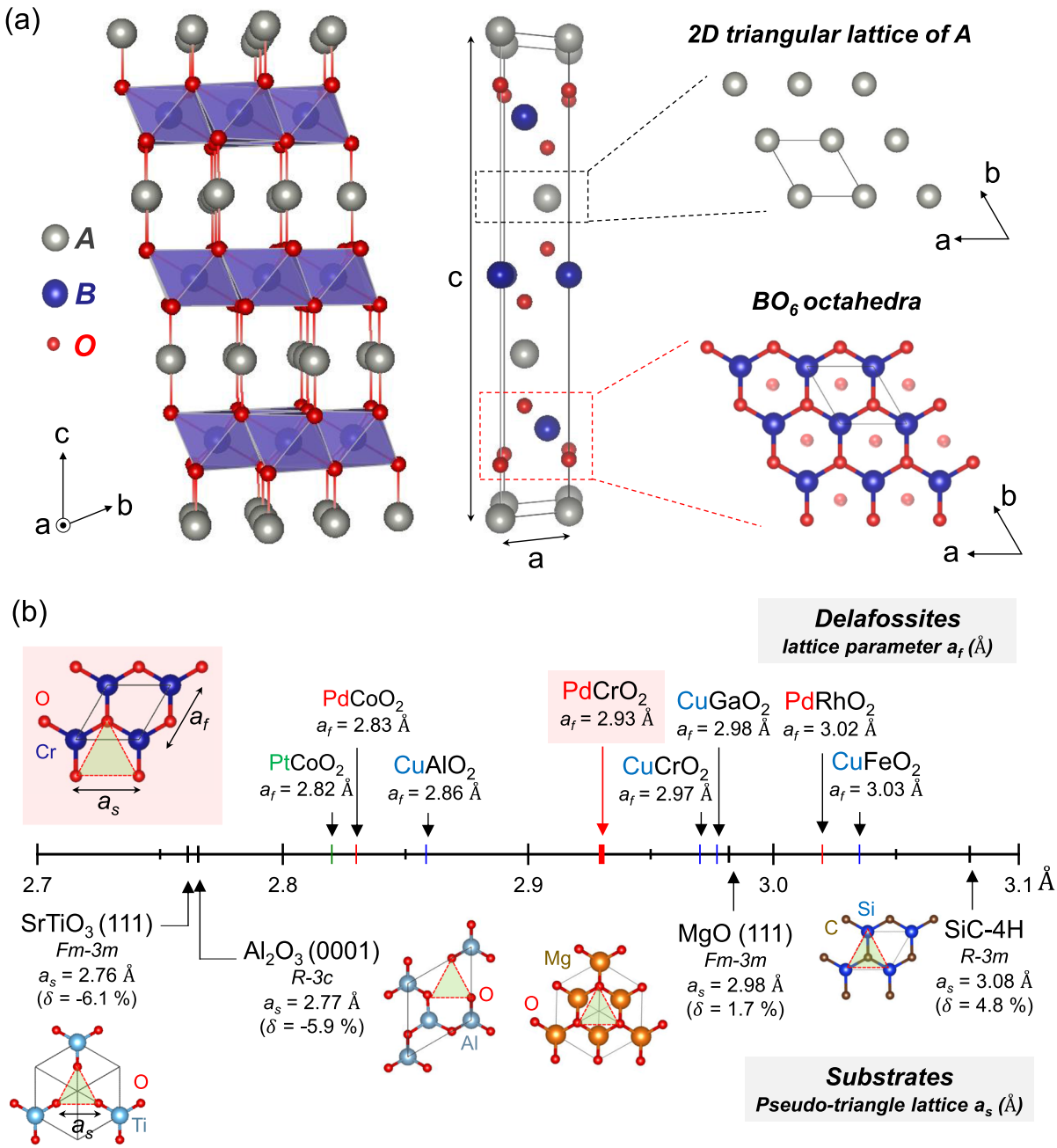

FIG. 1. (a) Crystal structure of the delafossite ABO_2 (space group R-3m). *A*, *B*, and O atoms are colored silver, blue, and red, respectively. The stacked layers of closed-packed *A* and edge-sharing BO_6 octahedra are also shown. (b) Schematic of the BO_6 octahedral surface of the delafossite structure and lattice parameters (top-left corner). Number line shows the lattice parameters of substrates (a_S) and delafossite buffer layer materials (a_f). Note that the surface lattice sizes (a_S) of the (111)-oriented cubic substrates are taken as a triangular unit to compare with the oxygen lattice of the delafossite, as shown in the triangular crystal face of each substrate.

A = Cu, Ag are semiconductors and have long been studied as *p*-type transparent conducting oxides.[6,7] This characteristic is in contrast to delafossites with *A* = Pd or Pt, which are highly metallic and exhibit conductivities as high as copper.[3,4,8] Furthermore, the triangular in-plane connectivity gives rise to non-collinear antiferromagnetic states for materials, such as $CuFeO_2$,[9] $CuCrO_2$,[10] $AgNiO_2$,[11] and $PdCrO_2$.[12] While several interesting studies were reported from bulk materials, including large magnetoresistance,[13] unconventional anomalous Hall effect,[14,15] field-induced magnetic transition,[9,11] and magnetoelectric effect,[16,17] many interesting

questions, including the strain tuning, proximity effect, and dimensional control of interlayer coupling, are yet to be understood as there have been only a few attempts on the epitaxial growth of metallic delafossites.[18–21] Among delafossites, $PdCrO_2$ is highly attractive owing to the strong coupling between highly conducting Pd 2D layers and CrO_2 non-collinear antiferromagnetic layers and, consequently, exhibits unusual transport properties.[14,15,22,23] However, due to the volatile nature of PdO and deleterious nucleation of impurity phases that are hard to avoid,[19,20] the successful growth of the Pd-based delafossites remains yet to be achieved.

Here, we have systematically studied the epitaxial synthesis of the delafossite $PdCrO_2$ by pulsed laser epitaxy (PLE) on various substrates. By systematically tuning the growth conditions, mainly including growth temperature (T), oxygen partial pressure (P_{O_2}), and laser fluence (J), it was found that the formation of high-quality, phase pure $PdCrO_2$ epitaxial films requires a delicate balance of the growth conditions. Although the growth conditions that favor the growth of $PdCrO_2$ are nominally independent of the substrate, the highest quality $PdCrO_2$ was found to grow on low-lattice-mismatched delafossite buffer layers, which significantly reduced the appearance of impurity phases. The quality of the buffer layer was found to be the limiting factor for the growth of $PdCrO_2$, which indicates that further improvement of the buffer layer or development of a new generation of bulk crystals will ultimately enable synthesis of high quality $PdCrO_2$ epitaxial thin films.

The pulsed-laser epitaxy of $PdCrO_2$ films used a sintered polycrystalline target. Based on the previous reports on bulk synthesis,[2,24] the polycrystalline $PdCrO_2$ target was prepared using a combination of Pd, $PdCl_2$, and $LiCrO_2$. These powders were mixed in a stoichiometric ratio and then sintered at 900 °C in a vacuum furnace, which resulted in $PdCrO_2$ mixed with LiCl. The mixture was then ground and washed with distilled water for 30 min to remove the LiCl byproduct. Note that LiCl is highly soluble in water, unlike $PdCrO_2$. The resulting $PdCrO_2$ polycrystalline powder was then dried by heating to 120 °C in air for approximately 12 h. This powder was then pelletized and sintered at 800 °C in atmosphere to form the final target. For the $PdCrO_2$ single crystal, a mixture of the obtained polycrystalline $PdCrO_2$ and NaCl flux were annealed at 900 °C for 24 h and slowly cooled to 800 °C as described elsewhere.[15,24] We used single crystals to compare the optical properties with our thin films. For the film growth, the growth conditions were widely varied (T = 500–800 °C, P_{O_2} = 10–1000 mTorr, and J = 1–2 J/cm^2), whereas the repetition rate of the KrF excimer laser (λ = 248 nm) was fixed at 10 Hz. After the growth, the samples were cooled to room temperature in P_{O_2} = 100 Torr. $CuCrO_2$ thin films, used as a buffer layer, were grown directly on Al_2O_3 at T = 700 °C under an oxygen pressure of P_{Otext2} = 10 mTorr. We note that the epitaxy of $CuCrO_2$ films was quite straightforward and can be readily achieved over a wide growth window. Thus, as the growth of $PdCrO_2$ was difficult, we used $CuCrO_2$ to see if the use of a buffer layer with the same crystal structure would facilitate the nucleation of $PdCrO_2$. The crystal structure was characterized by x-ray diffraction (XRD) using a four-circle high-resolution x-ray diffractometer (X'Pert Pro, PANalytical; Cu $K\alpha_1$ radiation), and the thickness of the film (d) was calibrated by x-ray reflectivity (XRR). The surface morphology measurements were taken by atomic force microscopy (Veeco Dimension 3100). High-angle annular dark-field scanning transmission electron microscopy (HAADF-STEM) images were collected using a fifth order aberration-corrected NION UltraSTEM 200 operated at 200 kV using a 30 mrad convergence semi-angle. The transport properties were measured using the van der Pauw configuration with a 14 T Quantum Design PPMS using aluminum wires directly wire-bonded to the $PdCrO_2$ films. Optical properties of $PdCrO_2$ thin films, the $PdCrO_2$ single crystal, and the $SrTiO_3$ substrate were measured using spectroscopic ellipsometry for UV-visible range (M-2000, J.A. Woollam Co.) with photon energies between 0.74 eV and 5.86 eV at an incident angle of 65°. For films and substrates, infrared ellipsometry (IR-VASE, J.A. Woollam) was used for energy below 0.74 eV. The spectra were fitted using a two-layer model (film/substrate) to obtain physically reasonable dielectric functions. For the single crystal, the complex optical conductivity was extracted using the Kramers–Kronig analysis after measuring the near-normal reflectance (Vertex 80v FT-IR spectrometer, Bruker).

$PdCrO_2$ has a rhombohedral structure (space group R-3m) with lattice parameters of $a = b$ = 2.930 Å and c = 18.087 Å ($\alpha = \beta = 90°$, $\gamma = 120°$).[1,12] The triangular in-plane geometry requires the use of substrates with a triangular (hexagonal) symmetry. This lattice symmetry can be obtained from the same crystallographic structure or (111) oriented cubic perovskites that are available with a wide range of lattice constants. As shown in Fig. 1(b), we chose (111)-$SrTiO_3$, (0001)-Al_2O_3, (111)-MgO, and (0001)-4H-SiC. We note that there have been reports on successful synthesis of bulk materials, including $CuCrO_2$, $CuAlO_2$, $CuFeO_2$, $CuGaO_2$, $PdCoO_2$, $PdRhO_2$, and $PtCoO_2$.[1,2] Among them, a few Cu-based delafossites, including $CuAlO_2$[6] and $CuCrO_2$,[25] were successfully grown as thin films. In Fig. 1(b), we compare lattice parameters of various delafossites and commercially available single crystals as potential buffer layers or substrates. The lattice mismatches [$\delta(\%) = (a_s - a_f)/a_s \times 100$, where a_s is the lattice parameter of the substrate] of $PdCrO_2$ (a_{PCO} = 2.930 Å) with various substrates are indicated in parentheses. Note that the surface lattice size (a_S) of the (111)-oriented cubic substrates is taken as a triangular unit to interact with the oxygen lattice of the delafossite, as illustrated in Fig. 1(b). Overall, this approach gives a wide range of lattice mismatches, i.e., (111)-$SrTiO_3$ (δ = −6.1%), (0001)-Al_2O_3 (δ = −5.9%), (111)-MgO (δ = 1.7%), and 4H-SiC (δ = 4.8%). The majority of previous studies of thin-film growth of delafossites have focused on Al_2O_3 (0001) as a substrate due to its close lattice match and the hexagonal symmetry as well as the chemical similarity of the oxygen terminated surface of Al_2O_3 to the BO_2 terminating surface of the delafossites. Thus, our wide selection of substrates allows us to study the influence of strain in achieving high-quality delafossite films.

To understand the role of the substrate in nucleation of both the delafossite and the impurity phases, we grew $PdCrO_2$ films on the substrates mentioned earlier, as well as on an additional buffer layer, i.e., single-monolayer PLE-grown $CuCrO_2$ (δ = 1.3%) (~0.6 nm in thickness) on (0001) Al_2O_3. Initial growth parameters were optimized for $PdCrO_2$ films grown on Al_2O_3, i.e., P_{O_2} = 100 mTorr, T = 700 °C, and J = 1.5 J/cm^2. XRD 2θ–θ scans for ~30 nm thick $PdCrO_2$ films grown under the same optimum conditions on all of the substrates and buffer layers are shown in Fig. 2(a). As one can find, the strong appearance of the 0006 $PdCrO_2$ peak indicates that the $PdCrO_2$ phase is well-established. The most intense $PdCrO_2$ peaks occur for the substrates and buffer layers with the

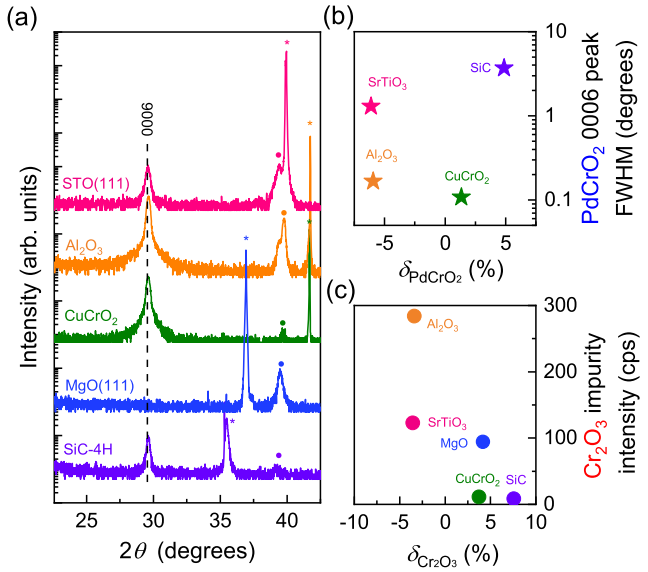

FIG. 2. (a) XRD scans of $PdCrO_2$ thin films grown on four different substrates [STO (111), Al_2O_3, MgO (111), and SiC_4H] and a $CuCrO_2$ buffer layer. The latter buffer layer was grown on an Al_2O_3 substrate. The peaks from $PdCrO_2$ thin films, substrates, and Cr_2O_3 impurity are marked with a dotted line, asterisks (*), and solid dots (●), respectively. (b) Crystallinity of films represented as the full width half maximum (FWHM) of the $PdCrO_2$ 0006 peak as a function of the lattice mismatch of $PdCrO_2$, $\delta_{PdCrO_2}(\%) = (a_s - a_{PdCrO_2})/a_s \times 100$. (c) XRD intensity of the Cr_2O_3 impurity peak as a function of the lattice mismatch of Cr_2O_3, $\delta_{Cr_2O_3}(\%) = (a_s - a_{Cr_2O_3})/a_s \times 100$.

closest lattice match, Al_2O_3 and delafossite $CuCrO_2$ buffer layer. The $PdCrO_2$ peaks are suppressed, in general, as the lattice mismatch increases. Despite a small mismatch, no sign of $PdCrO_2$ film peaks was observed on MgO substrates. The full width at half maximum (FWHM) from the XRD rocking curve ω-scans measured for the 0006 peak is plotted as a function of the lattice mismatch in Fig. 2(b). This result shows similar dependence on the lattice mismatch. For films grown with a low mismatch, the rocking curve width is rather low, ~0.1° (Al_2O_3 and $CuCrO_2$), whereas FWHM values of up to >1° are found for 4H-SiC and $SrTiO_3$. We also note that, while the sign is opposite, $PdCrO_2$/SiC ($\delta = 4.8\%$) has a similar size of the lattice mismatch with $PdCrO_2/Al_2O_3$ ($\delta = -5.9\%$), but the FWHM of $PdCrO_2$ phases show a huge difference. This may be because the tensile strain increases oxygen deficiency due to the reduced formation energy or increased oxygen exchange kinetics.[26–28]

The role the substrate plays in nucleation can be additionally seen by comparing the intensity of secondary phases. Specifically, in Fig. 2(c), the intensity of the Cr_2O_3 peak at 39.7° is plotted as a function of the lattice mismatch. The films grown on a buffer layer of $CuCrO_2$ and on 4H-SiC showed highly suppressed Cr_2O_3 impurity phases, whereas films grown on Al_2O_3, $SrTiO_3$, and MgO showed Cr_2O_3 peaks with a much larger intensity. This XRD result shows that the nucleation of Cr_2O_3 does not solely depend on the lattice mismatch, but rather is highly dependent on the crystal structure of the substrate. Specifically, Cr_2O_3 shares the same crystal structure as that of Al_2O_3 and, thus, seems very energetically favorable to form epitaxially on Al_2O_3, explaining the dominant formation of Cr_2O_3. This result further contrasts with films grown on both buffer layer and 4H-SiC, where there is only a very weak Cr_2O_3 peak, likely indicating that the formation of the Cr_2O_3 phase is unfavorable on these surfaces. In addition to the crystallographic symmetry, we further note that the formation of Cr_2O_3 impurities might be suppressed by preventing the loss of volatile PdO by using, for instance, Pd-rich targets as demonstrated for $PdCoO_2$.[18]

In general, for heteroepitaxy, the closer the film and the substrate crystal structures to one another, the higher the film quality thereon. For example, $PdCoO_2$ films grown on Al_2O_3 have shown epitaxial twins due to multiple ways to crystallographically connect the delafossite structure to the corundum structure.[18–20] As data in Fig. 2 show, the $CuCrO_2$ delafossite buffer layer gives rise to the highest crystalline quality $PdCrO_2$. In addition to the small lattice mismatch and identical crystal symmetry of R-3m, $CuCrO_2$ is electrically insulating, which readily allows transport measurements of $PdCrO_2$.

Thin film of $CuCrO_2$ was grown using PLE on Al_2O_3 at $T = 700\,^{\circ}C$, $P_{O_2} = 10$ mTorr, and $J = 1.5$ J/cm^2. An XRD scan is shown in Fig. 3(a) for $CuCrO_2$ where the delafossite 0003n peaks are the only peaks resolved. Moreover, the rocking curve FWHM of the 0006 peak from a thick $CuCrO_2$ film (10 nm) is ~0.1°, indicating a higher film quality than those in previous reports.[29] Using a single monolayer $CuCrO_2$ buffer layer, the growth conditions of $PdCrO_2$ were further mapped systematically. Figure 3(b) shows a full XRD scan and an ω-rocking curve for a $PdCrO_2$ film grown under optimum conditions, which confirms a good epitaxy of $PdCrO_2$.

Figure 3(c) summarizes the results for $PdCrO_2$ films grown at different T and P_{O_2}, where the contour plot indicates the rocking curve FWHM values of the 0006 $PdCrO_2$ peak, and the symbols indicate whether the sample is metallic (solid green circles) or insulating (blue stars). The conditions, where there were no $PdCrO_2$ peaks observed, are marked with red crossed circles. From these data, the optimum growth regime is found to reside in $600\,^{\circ}C \le T \le 700\,^{\circ}C$ and 200 mTorr $\le P_{O_2} \le$ 300 mTorr. Within this optimal growth window, the rocking curve width is minimal, and the films are metallic, whereas the films grown outside of the optimal window are found to be totally insulating (beyond our instrumental limit) even in the case with good crystallinity. The insulating nature was found to be extrinsic as islands were rather dominantly grown instead of a continuous film. The rocking curve width ($\Delta\omega = 0.1°$) is nominally the same as the underlying $CuCrO_2$, which indicates that the structural quality is largely limited by the underlying buffer layer. Finally, it is important to point out that these growth conditions are nominally identical to those found for $PdCrO_2$ directly grown on Al_2O_3, which confirms that the formation of the impurities is entirely driven by the character of the surface. In addition, as shown in Fig. 3(d), the XRD reciprocal space mapping confirmed that this film is fully strained. The HAADF-STEM image shown in Fig. 3(e) for $PdCrO_2$ grown on a single-unit-cell thick $CuCrO_2$ buffered Al_2O_3 substrate further confirms the high crystallinity of the epitaxial thin film. From this image taken along the $\langle\bar{1}100\rangle$ direction, the layered delafossite crystalline structure with alternatively stacked Pd (bright) and Cr (less bright) layers is clearly resolved on the Al_2O_3 substrate, which is the darker region on the bottom of the image. The atomic structure at the interface is resolvable, for which there are several interesting aspects: First, the nucleation layer on the Al_2O_3 substrate turns out to be the Cr–O sublayer, followed by stacking of the Pd sublayer,

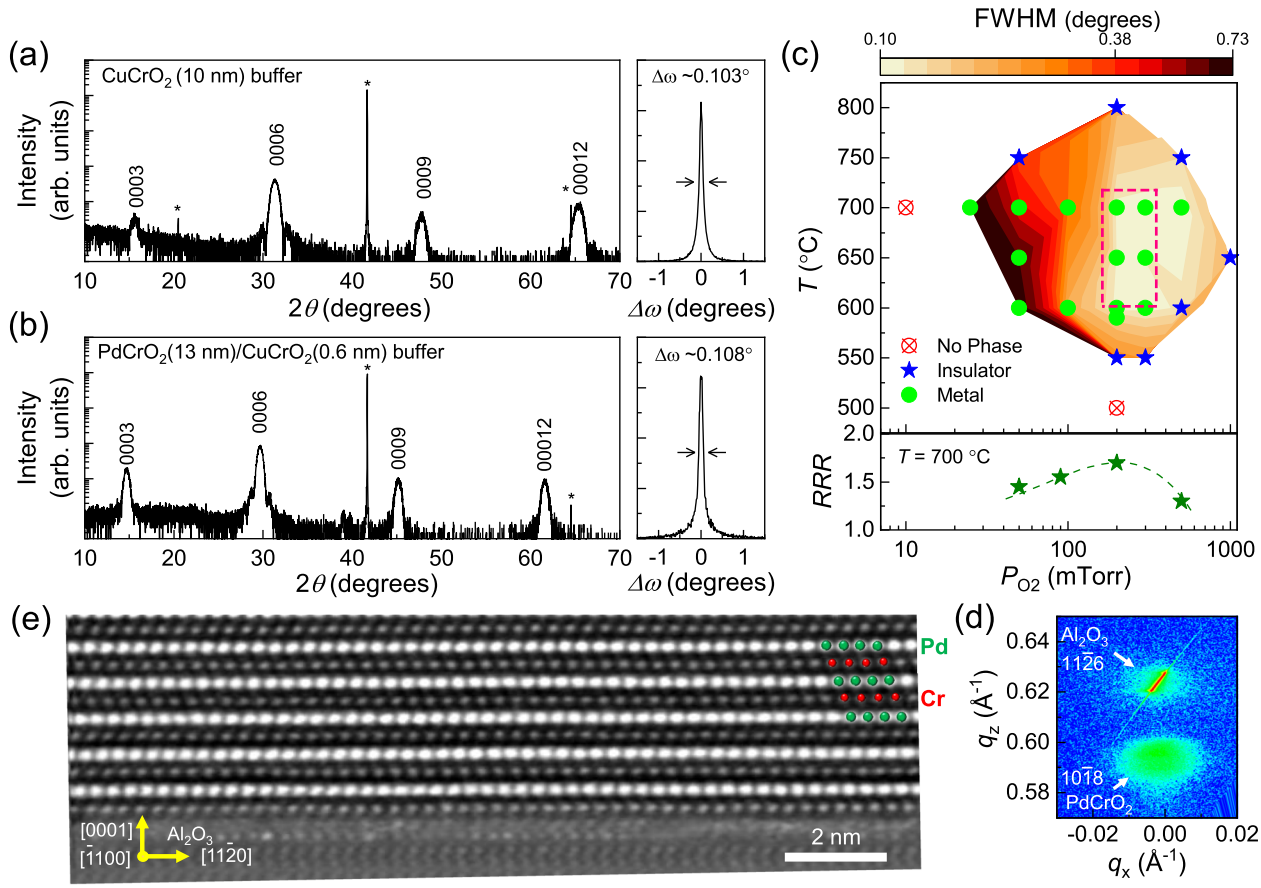

FIG. 3. (a) XRD 2θ-θ scans of a $CuCrO_2$ thin film (thickness 10 nm) grown on an Al_2O_3 (0001) substrate under optimum growth conditions (left). The individual 0003*n* delafossite peaks are indicated, while the substrate is indicated by an asterisk (*). The corresponding rocking curve for the $CuCrO_2$ 0006 peak is shown on the right. (b) XRD 2θ-θ scans of a $PdCrO_2$ thin film (thickness 13 nm) grown on a $CuCrO_2$ buffer layer (left). The corresponding rocking curve for the $PdCrO_2$ 0006 peak is shown on the right. (c) Contour plot of FWHM of the $PdCrO_2$ 0006 peak as functions of oxygen partial pressures, P_{O_2}, and growth temperature, *T*, showing the optimal growth window (top) and oxygen partial pressure dependence of the residual resistivity ratio (RRR) (bottom). A larger RRR value was achieved within the optimal growth window. (d) XRD reciprocal space map of a 23.5-nm-thick film recorded around the Al_2O_3 11$\bar{2}$6 reflection and the $PdCrO_2$ 10$\bar{1}$8 reflection. (e) A cross-sectional HAADF-STEM image of a $PdCrO_2$ thin film, showing that the Cr–O layer is the first nucleation layer formed on the substrate surface. We note that, while a monolayer-thick $CuCrO_2$ buffer layer was used, we could not find a clear signature of Cu at the interface. We further note that a couple of layers at the interface of the substrate reveal some structural and chemical disorder that might stem from the buffer layer growth. See the text for a more detailed explanation.

due to the triangular symmetry of the CrO_6 layer. Second, as Cu (atomic number $Z = 29$) is much lighter than Pd ($Z = 46$), the growth of the $CuCrO_2$ buffer layer should be manifested by appearance of the less bright Cu layer than that of Pd on top of Cr–O (note the STEM brightness $\approx Z^2$). However, we found no obvious sign of the Cu layer from our *Z*-contrast imaging. This result might be due to the fact that the first top Cu layer was replaced or mixed with Pd instead of nucleation of a Cr–O layer on top of the Cu layer. Third, the substrate side of the lattices shows a sign of disorder that might originate from intermixing with the film. Nevertheless, the overall structure seems well-maintained without a hint of severe structural disorder or impurity phases. This can be further understood by more extensive studies utilizing element-specific atomic resolution electron energy loss spectroscopy (EELS), which we leave out as a future study.

Figure 4 shows the thickness dependent transport data for the $PdCrO_2$ films grown on $CuCrO_2$ buffered Al_2O_3. As shown in Fig. 4(a), our films ($d = 3.6$–33 nm in thickness) show clear metallic behaviors, except for the thinnest ($d = 3.6$ nm) film, of which $\rho(T)$ shows a slight upturn at low temperature, consistent with the onset of a localization transition. Below 3.6 nm, $PdCrO_2$ thin films were no longer conducting due to the finite thickness, typical of conducting oxides such as $SrRuO_3$.[30,31] $\rho(T)$ for $PdCrO_2$ films was nearly independent of the thickness above ~4 nm, but the value was about an order of magnitude higher ($\rho = 100\ \mu\Omega$ cm at 300 K) than that of a single crystal ($\rho_{single} = 8.2\ \mu\Omega$ cm). The overall quality of the films is captured by the residual resistivity ratio (RRR, the ratio of the room temperature ρ to the low temperature ρ). The maximum RRR value is 2.1 for the 33-nm-thick film. This value is comparable to other $PdCoO_2$ thin films grown by pulsed laser deposition,[18] but

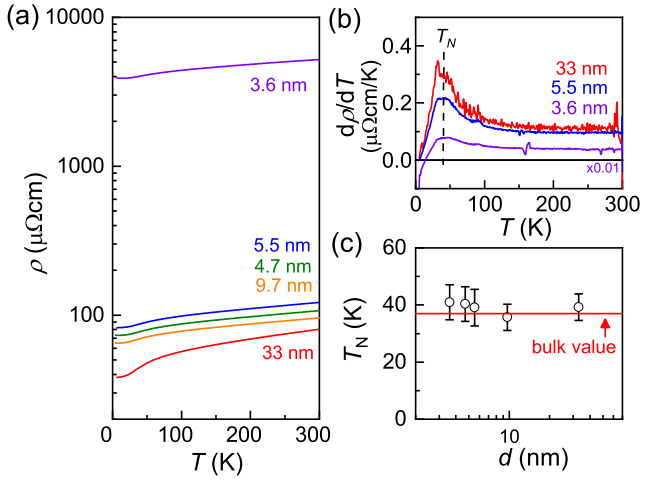

FIG. 4. (a) Temperature dependent resistivity of $PdCrO_2$ thin films with various thicknesses of 3.6–33 nm. (b) Temperature dependent $d\rho/dT$ data, which show clear kinks at T_N = ~37 K. (c) The antiferromagnetic ordering temperature (T_N) from $PdCrO_2$ films with different film thicknesses shows a good agreement with the bulk value.

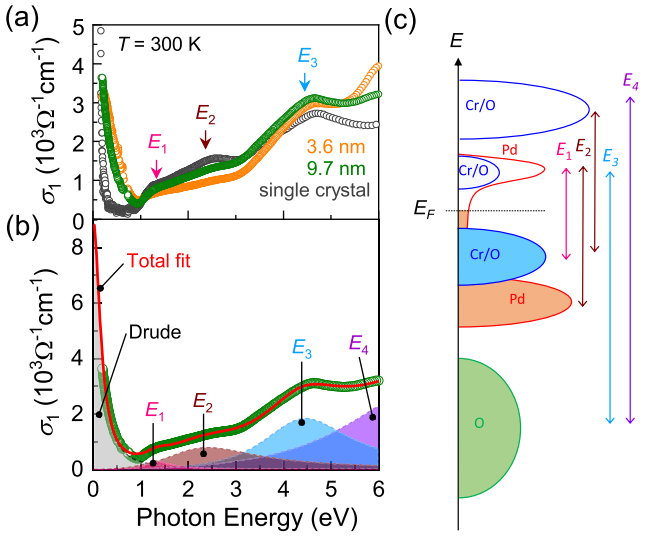

FIG. 5. (a) Thickness dependent optical conductivity of $PdCrO_2$ thin films and single crystal, and (b) the corresponding fit is composed of a Drude term (gray colored area) and several Lorentzian features (E_1, E_2, E_3, E_4; colored areas). (c) Schematic DOS for $PdCrO_2$ based on a reported DFT calculation in Ref. 32. The expected optical transitions are denoted as E_1, E_2, E_3, and E_4.

significantly smaller than that from bulk crystals (RRR ~ 200).[15,24] This comparison indicates that the film quality may have room for further improvement. $\rho(T)$ also gives insight into the magnetic properties of $PdCrO_2$ films. Bulk $PdCrO_2$ exhibits non-collinear antiferromagnetism with a Néel temperature of T_N = 37.5 K,[12,24] which is reflected in transport measurements as a kink in $\rho(T)$.[15,24] This feature is more clearly seen in $d\rho(T)/dT$ shown in Fig. 4(b). We assign the maximum value of $d\rho/dT$ to be T_N and have plotted it as a function of thickness as shown in Fig. 4(c). These values are nominally thickness-independent over 3.6–33 nm at $T_N \approx 37$ K within the estimated error of around ±5 K, which agrees well with the bulk value.

Finally, optical conductivity spectra [$\sigma_1(\omega)$] of $PdCrO_2$ thin films and a single crystal at the room temperature are shown in Figs. 5(a) and 5(b), which were extracted from spectroscopic ellipsometry. Overall, $\sigma_1(\omega)$ of the thin films show a consistent behavior with that of the single crystal. First, all films and single crystal exhibited a low-energy Drude peak below around 1 eV, which reflects the metallic nature. They also showed several interband transitions at 1.3 (referred to as E_1), 2.3 (E_2), 4.5 (E_3), and above 6.0 eV (E_4). From electronic structure calculations,[32] a schematic density of states (DOS) is provided as shown in Fig. 5(c). From the schematic, the E_1 peak at 1.3 eV can be attributed to the on-site d–d transition between the hybridized Cr orbital states, and the E_2 peak at 2.3 eV to the d–d transition between the hybridized Cr or Pd orbital states. The E_3 and E_4 peaks at ~4.5 and above 6 eV are attributed to the charge transfer transition from the O to the Cr or Pd states. By considering the Drude and Lorentz oscillators, we fitted $\sigma_1(\omega)$ as shown in Fig. 5(b). The Drude parameters obtained from the fit were plasma frequency, $\omega_p \approx 28\,000$ cm^{-1}, and scattering rate, $\gamma_i \approx 1450 \pm 50$ cm^{-1} (wavenumber). We note that ω_p of our thin film is in good agreement with that of our $PdCrO_2$ single crystal ($\omega_p \approx 35\,000$ cm^{-1}, $\gamma_i \approx 220$ cm^{-1}) and a sister compound $PdCoO_2$ single crystal ($\omega_p \approx 33\,000$ cm^{-1}, $\gamma_i \approx 97$ cm^{-1}),[33] but the value of γ_i is 7–15 times larger than that from the single crystal. The obtained Drude parameters are summarized in Table I. The huge difference of γ_i is consistent with the higher resistivity of thin films. The Drude parameters were converted into relaxation time of $\tau \approx 3.65 \times 10^{-15}$ s, carrier density of $n_{3D}{}^{opt} \approx 1.3 \times 10^{22}$ cm^{-3}, mobility of $\mu^{opt} \approx 5.27 \pm 0.5$ cm^2/V s, and DC conductivity of $\sigma^{opt} \approx 9000\ \Omega^{-1}$ cm^{-1}, corresponding to $\rho^{opt} \approx 110\ \mu\Omega$ cm. The obtained values were consistent with the values from transport measurements. The data were found to be nominally thickness-independent, which indicates that the broad electronic properties are preserved down to the thinnest sample. The Drude parameters, however, show clear thickness dependence as listed in Table I. The scattering rate γ_i increases as the film thickness decreases. This finding implies that disorder may play a dominant role in the ultrathin limit. We also note that the optical conductivity, $\sigma_1(0)$, and DC conductivity, σ_{DC}, show a significant difference for the 3.6 nm-thick sample. We attribute this difference to potential inhomogeneity, e.g., twin boundaries and Cr_2O_3 impurity phases in the vicinity of the interface.

In summary, we have shown that, albeit on the border of instability, $PdCrO_2$ can be grown epitaxially by pulsed laser epitaxy. Epitaxial strain and the chemical and structural characteristics of the substrate are of key importance to the phase purity of $PdCrO_2$. However, substrates that are at low strain states yet closely match impurity phases strongly enhance the formation of these secondary phases. As such, achieving epitaxial $PdCrO_2$ films required a different approach. We found that the use of a $CuCrO_2$ buffer layer as thin as a single monolayer not only helped reduce the impurity phases but also improved the crystalline quality of the films in comparison to the films grown directly on Al_2O_3. $PdCrO_2$ epitaxial thin films exhibited a clear magnetic transition down to 3.6 nm. Overall, our results show that overcoming these significant growth challenges for this family of materials is the first step toward a new

TABLE I. The Drude model parameters of $PdCrO_2$ thin films fitted to the optical conductivity and DC conductivity, which are compared to the values from a $PdCrO_2$ single crystal. Literature values for a $PdCoO_2$ single crystal is also shown as a comparison.

		ω_p (cm^{-1})	γ_i (cm^{-1})	$\sigma_1(0)$ (Ω^{-1} cm^{-1})	σ_{DC} (Ω^{-1} cm^{-1})
$PdCrO_2$ thin film	3.6 nm	25 000	3310	4.5×10^3	0.2×10^3
	5.5 nm	28 000	2260	6×10^3	8.3×10^3
	9.7 nm	28 000	1450	9×10^3	9.1×10^3
$PdCrO_2$ single crystal		35 000	220	0.8×10^5	1.22×10^5
$PdCoO_2$ single crystal[33]		33 000	97	1.85×10^5	3.84×10^5

generation of complex oxide thin films and creation of novel quantum heterostructures.

This work was supported by the U.S. Department of Energy, Office of Science, Basic Energy Sciences, Materials Sciences and Engineering Division. The transport measurement and analysis were supported by the Computational Materials Sciences Program, and the optical measurement and analysis by W.S.C. was supported by the Basic Science Research Program through the National Research Foundation of Korea (Grant No. NRF-2019R1A2B5B02004546). C.S. was supported in part for obtaining the single crystal optical data by the Creative Materials Discovery Program through the National Research Foundation of Korea (NRF) funded by the Ministry of Science and ICT (Grant No. NRF-2017M3D1A1040828). Single crystal optical measurements were performed using facilities at the IBS Center for Correlated Electron Systems, Seoul National University.

REFERENCES

[1] C. T. Prewitt, R. D. Shannon, and D. B. Rogers, Inorg. Chem. **10**, 713–718 (1971).
[2] D. B. Rogers, R. D. Shannon, C. T. Prewitt, and J. L. Gillson, Inorg. Chem. **10**, 719–723 (1971).
[3] C. W. Hicks, A. S. Gibbs, A. P. Mackenzie, H. Takatsu, Y. Maeno, and E. A. Yelland, Phys. Rev. Lett. **109**, 116401 (2012).
[4] P. J. W. Moll, P. Kushwaha, N. Nandi, B. Schmidt, and A. P. Mackenzie, Science **351**, 1061 (2016).
[5] A. P. Mackenzie, Rep. Prog. Phys. **80**, 032501 (2017).
[6] H. Kawazoe, M. Yasukawa, H. Hyodo, M. Kurita, H. Yanagi, and H. Hosono, Nature **389**, 939–942 (1997).
[7] H. Yanagi, S. I. Inoue, K. Ueda, H. Kawazoe, H. Hosono, and N. Hamada, J. Appl. Phys. **88**, 4159 (2000).
[8] P. Kushwaha, V. Sunko, P. J. Moll, L. Bawden, J. M. Riley, N. Nandi, H. Rosner, M. P. Schmidt, F. Arnold, E. Hassinger, T. K. Kim, M. Hoesch, A. P. MacKenzie, and P. D. King, Sci. Adv. **1**, e1500692 (2015).
[9] T. Kimura, J. C. Lashley, and A. P. Ramirez, Phys. Rev. B **73**, 220401 (2006).
[10] H. Kadowaki, H. Kikuchi, and Y. Ajiro, J. Phys.: Condens. Matter **2**, 4485–4493 (1990).
[11] A. I. Coldea, L. Seabra, A. McCollam, A. Carrington, L. Malone, A. F. Bangura, D. Vignolles, P. G. Van Rhee, R. D. McDonald, T. Sörgel, M. Jansen, N. Shannon, and R. Coldea, Phys. Rev. B **90**, 020401 (2014).
[12] H. Takatsu, H. Yoshizawa, S. Yonezawa, and Y. Maeno, Phys. Rev. B **79**, 104424 (2009).
[13] H. Takatsu, J. J. Ishikawa, S. Yonezawa, H. Yoshino, T. Shishidou, T. Oguchi, K. Murata, and Y. Maeno, Phys. Rev. Lett. **111**, 056601 (2013).
[14] H. Takatsu, S. Yonezawa, S. Fujimoto, and Y. Maeno, Phys. Rev. Lett. **105**, 137201 (2010).
[15] J. M. Ok, Y. J. Jo, K. Kim, T. Shishidou, E. S. Choi, H. J. Noh, T. Oguchi, B. I. Min, and J. S. Kim, Phys. Rev. Lett. **111**, 176405 (2013).
[16] K. Kimura, H. Nakamura, S. Kimura, M. Hagiwara, and T. Kimura, Phys. Rev. Lett. **103**, 107201 (2009).
[17] K. Kimura, H. Nakamura, K. Ohgushi, and T. Kimura, Phys. Rev. B **78**, 140401 (2008).
[18] T. Harada, K. Fujiwara, and A. Tsukazaki, APL Mater. **6**, 046107 (2018).
[19] M. Brahlek, G. Rimal, J. M. Ok, D. Mukherjee, A. R. Mazza, Q. Lu, H. N. Lee, T. Z. Ward, R. R. Unocic, G. Eres, and S. Oh, Phys. Rev. Mater. **3**, 093401 (2019).
[20] P. Yordanov, W. Sigle, P. Kaya, M. E. Gruner, R. Pentcheva, B. Keimer, and H. U. Habermeier, Phys. Rev. Mater. **3**, 085403 (2019).
[21] J. Sun, M. R. Barone, C. S. Chang, M. E. Holtz, H. Paik, J. Schubert, D. A. Muller, and D. G. Schlom, APL Mater. **7**, 121112 (2019).
[22] S. Arsenijević, J. M. Ok, P. Robinson, S. Ghannadzadeh, M. I. Katsnelson, J. S. Kim, and N. E. Hussey, Phys. Rev. Lett. **116**, 087202 (2016).
[23] S. Ghannadzadeh, S. Licciardello, S. Arsenijević, P. Robinson, H. Takatsu, M. I. Katsnelson, and N. E. Hussey, Nat. Commun. **8**, 15001 (2017).
[24] H. Takatsu and Y. Maeno, J. Cryst. Growth **312**, 3461 (2010).
[25] D. Li, X. Fang, Z. Deng, S. Zhou, R. Tao, W. Dong, T. Wang, Y. Zhao, G. Meng, and X. Zhu, J. Phys. D: Appl. Phys. **40**, 4910 (2007).
[26] J. R. Petrie, H. Jeen, S. C. Barron, T. L. Meyer, and H. N. Lee, J. Am. Chem. Soc. **138**, 7252–7255 (2016).
[27] T. L. Meyer, R. Jacobs, D. Lee, L. Jiang, J. W. Freeland, C. Sohn, T. Egami, D. Morgan, and H. N. Lee, Nat. Commun. **9**, 92 (2018).
[28] J. R. Petrie, C. Mitra, H. Jeen, W. S. Choi, T. L. Meyer, F. A. Reboredo, J. W. Freeland, G. Eres, and H. N. Lee, Adv. Funct. Mater. **26**, 1564–1570 (2016).
[29] D. Shin, J. S. Foord, R. G. Egdell, and A. Walsh, J. Appl. Phys. **112**, 113718 (2012).
[30] D. Toyota, I. Ohkubo, H. Kumigashira, M. Oshima, T. Ohnishi, M. Lippmaa, M. Takizawa, A. Fujimori, K. Ono, M. Kawasaki, and H. Koinuma, Appl. Phys. Lett. **87**, 162508 (2005).
[31] A. Rastogi, M. Brahlek, J. M. Ok, Z. Liao, C. Sohn, S. Feldman, and H. N. Lee, APL Mater. **7**, 091106 (2019).
[32] D. Billington, D. Ernsting, T. E. Millichamp, C. Lester, S. B. Dugdale, D. Kersh, J. A. Duffy, S. R. Giblin, J. W. Taylor, P. Manuel, D. D. Khalyavin, and H. Takatsu, Sci. Rep. **5**, 12428 (2015).
[33] C. C. Homes, S. Khim, and A. P. Mackenzie, Phys. Rev. B **99**, 195127 (2019).